THE ASTROPHYSICAL JOURNAL, 372:54–66, 1991 May 1

THE DISTRIBUTION AND KINEMATICS OF NEUTRAL GAS IN M31

ROBERT BRAUN[1]
Netherlands Foundation for Research in Astronomy, Dwingeloo, The Netherlands, and National Radio Astronomy Observatory,[2] Socorro, New Mexico
Received 1990 August 3; accepted 1990 October 15

ABSTRACT

The kinematic signature of spiral arm segments in the highly inclined gaseous disk of M31 is identified within previously published data bases of neutral hydrogen emission. These features are tabulated to give a complete spatial and kinematic parameterization of the neutral gas distribution. Neither a fixed inclination nor a fully axisymmetric velocity field were assumed in the analysis. Significant variations in the local orientation are derived, including a systematic departure of the inner (2 kpc) disk to an orientation tilted by 15° with respect to the outer disk. The spatial distribution of gas is very well described by a global two-arm trailing spiral. The spiral in the inner 5 kpc has an elliptical distortion with an axial ratio of about 1.9 which is coaligned with the long axis of the apparently triaxial stellar bulge. Between 5.4 and 16.3 kpc the spiral pattern is logarithmic with pitch angle 6°.7. Beyond 17 kpc the two spiral arms merge into a single structure. The rotation curve, after correction for the inner ellipticity, is well fitted with just two mass components: a stellar bulge and disk with mass distributions which are traced by the blue light. A total mass $M = (2.0 \pm 0.1) \times 10^{11}\ M_{\odot}$ is found within 28 kpc. Ratios of mass to blue luminosity for *both* the bulge and disk are 6.5 $M_{\odot}/L_{\odot}$. There is no evidence for additional mass with a more uniform spatial distribution out to 28 kpc. Identifying the two boundaries of the range in radius over which the spiral is logarithmic with (1) the inner Lindblad resonance and (2) corotation leads to a pattern speed of 15 ± 2 km s^{-1} kpc^{-1} and a predicted outer Lindblad resonance at 22 kpc, where the two arms are observed to merge. The most obvious driver of the spiral pattern seems to be M32, which may also be responsible for many of the departures from a planar distribution as well as significant asymmetries in rotation velocity between 12 and 16 kpc radius. The radial dependence of gas scale height is found to be roughly linear, extending from about 200 pc at 5 kpc radius to about 600 pc at 25 kpc.

Subject headings: galaxies: individual (M31) — galaxies: internal motions — galaxies: interstellar matter — galaxies: structure — radio sources: 21 cm radiation

1. INTRODUCTION

Because of its proximity, M31 offers a unique opportunity for the detailed study of the physical processes at work in a normal late-type spiral galaxy. Recognition of this opportunity has led to an unparalleled observational assault, which continues to provide new light on a wide range of phenomena. However, some of the potential to address fundamental questions concerning galactic spiral structure, mass distributions, and many other issues is hampered by the "awkward" orientation of the galaxy. Since the mean galactic disk is only about 13° removed from the line of sight, and there are many indications for localized departures from the mean plane, it becomes difficult to assign a unique radius within the galaxy to positions not on the (local) major axis. On the other hand, the high mean inclination of the galactic disk provides a high degree of sensitivity to variations in inclination which might conceivably be exploited to study those variations. Assuming that such variations could be understood, it might then become possible to determine the three-dimensional distribution and kinematics of the disk.

There have been a number of discussions of the spatial distribution of gas and massive stars in M31, including those of Baade (1963), Arp (1964), Roberts (1966), Byrd (1978), Simien et al. (1978), Henderson (1979), Hodge (1979), Unwin (1980), Sofue & Kato (1981), Sawa & Sofue (1981), and Brinks & Burton (1984). In general, the workers faced with explaining neutral hydrogen data, in which multiple velocity components are observed along many lines of sight, have stressed the need to consider significant departures from a planar disk distribution. Optical observers, lacking this strong impetus, have generally held to the assumption of a fixed inclination in recent years, although Arp (1964) pointed out the likelihood of warping in the outer galaxy. An exception to this is the recent suggestion by Ciardullo et al. (1988) based on the roughly circular morphology of the ionized gas within about 5′ of the nucleus, that the gas in the inner galaxy is significantly more face-on than in the outer galaxy. In the current discussion we will fully relax the assumption of a plane-parallel distribution of gas.

A further assumption which is generally made in a kinematic analysis is that the gas orbits are circular. This will be inappropriate in cases where the gravitational potential seen by the gas is significantly nonaxisymmetric—for example, in the presence of a bar. Evidence for a bar within M31, while still not compelling, is quite suggestive. There is a well-documented twisting of the optical isophote major axis from the arcminute scale (e.g., Hodge & Kennicutt 1982) through the (sub-)arcsecond scale (Light, Danielson, & Schwarzschild 1974). Stark (1977) has interpreted this isophote twisting in terms of a barlike triaxial ellipsoidal bulge with an axial ratio between

[1] Current address: Netherlands Foundation for Research in Astronomy, Postbus 2, 7990 AA, Dwingeloo, The Netherlands.

[2] The National Radio Astronomy Observatory (NRAO) is operated by Associated Universities, Inc., under National Science Foundation Cooperative Agreement AST-8814515.

about 1.6 and 1.8 in the mean disk plane and a long-axis orientation of about 30° ± 15° to the south of the near-side minor axis. Two-dimensional gasdynamical calculations (e.g., Sanders & Huntley 1976; Mulder 1986) suggest that such a perturbation of the gravitational potential would lead to significant departures from the axisymmetric velocity field, especially inside and near the inner Lindblad resonance. Gas orbits near this radius are expected to be approximately elliptical with the same long-axis orientation as the bar. We will refrain from making assumptions regarding the axisymmetry in the velocity field to the extent that it is possible to do so, and in any event clearly state any assumptions which are made.

2. ANALYSIS OF THE DATA BASE

A number of recent surveys (Emerson 1974, hereafter E74; Cram, Roberts, & Whitehurst 1980; Brinks & Shane 1984, hereafter BS84; Braun 1990) of neutral hydrogen emission have together effectively delineated the projected distribution and kinematics of neutral gas in M31. Each of these surveys has its own strengths and weaknesses for various applications. For the purposes of global parameterization we will employ the good velocity coverage of BS84 in the inner galaxy and the wide field coverage of E74 in the outer galaxy.

2.1. *Identification of Spiral Arm Segments*

A striking aspect of position-velocity images made parallel to the major axis in these surveys (e.g., Fig. 8 of BS84) is the number of distinct quasi-linear features which pass through or near the (minor axis, systemic velocity) origin and terminate at extreme velocities in a more diffuse and flattened "cap." With the moderate resolution of BS84 (about 30″), virtually all emission is resolved into such components. The physical interpretation of these features is quite straightforward. A rotating cylinder segment, of radius R, as illustrated in Figure 1, will have a velocity signature

$$V = V_{\rm sys} + \Delta V_{\rm sys} + V_c(R) \sin i(R) \frac{X}{R} \tag{1}$$

in terms of the major-axis coordinate, X, and the inclination from face-on, i. Assuming locally (i.e., within a $\sim 60°$ interval in local azimuth of the galaxy) that V_c, the local rotation velocity, and the inclination are fixed, then this signature is a line through the (minor axis, systemic velocity) origin with slope

$$\frac{dV}{dX} = \frac{V_c(R) \sin i(R)}{R} . \tag{2}$$

If the cylinder has a finite thickness, ΔR, this will project into a width $\Delta X = \Delta R \cos \theta$, for the position angle θ in the local disk plane away from the $+X$ axis so that a widening is expected at extreme X where $\theta \sim 0$. A finite cylinder height, h, determines, together with the local inclination and cylinder width, the range in minor axis coordinate, Y, over which the feature will be visible:

$$\Delta Y = h \sin i + \Delta R \,|\sin \theta|\, \cos i . \tag{3}$$

The effect of shocks, due for example to a spiral density wave, on the observed velocity signature will be primarily a shift, $\Delta V_{\rm sys}$, of the velocity origin of the quasi-linear structure, except in the vicinity of the major axis, where the gradient, dV/dX, will also be affected. This can be seen by comparing Figures 10*a* and 10*b* of Visser (1980). For various reasons the measurement of arm segment velocity gradients will be confined to regions removed from the major axis, so that they should not be adversely affected by the presence of shocks.

Since velocity crowding due to geometrical turning points in a disk is confined to the region of widening at extreme velocities, the observed linear features can be confidently associated with either or both of actual density enhancements and local velocity turning points, i.e., spiral arm segments. This recognition allows a compact parameterization of the kinematic structure. The measured velocity gradients are listed in Table 1 for all unambiguous linear features (arm segments) discernible in Figure 8 of BS84 (at a resolution of 60″). The gradients dV/dX are listed for minor-axis offsets $-25\farcm2 \leq Y \leq 31\farcm2$ at intervals of $1\farcm2$. Measurement errors vary between about 1% at intermediate gradients ($dV/dX \sim 7$ km s^{-1} arcmin^{-1}) to 5% at the extreme values (1.5 and 95 km s^{-1} arcmin^{-1}). The best-defined values are indicated by exclamation marks in the table, while asterisks mark the positions where the arm segments, though poorly defined, had an estimated mean brightness in excess of 2.5 K. The velocity offsets, $\Delta V_{\rm sys}$, of arm segments at $X = 0$ with respect to an assumed systemic velocity $V_{\rm sys} = -315$ km s^{-1} are listed in Table 2. The accuracy to which these could be determined was about 5 km s^{-1}.

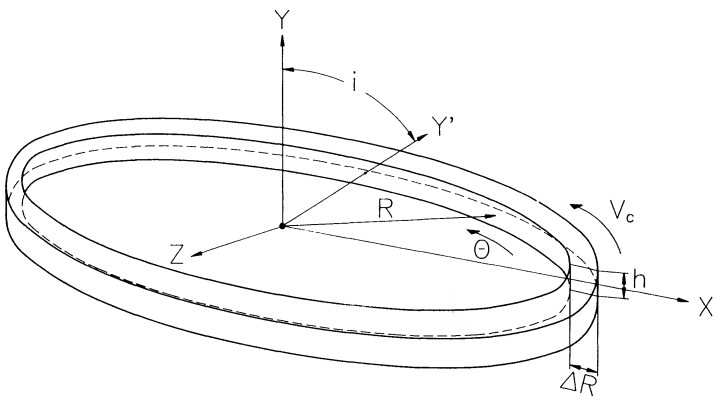

FIG. 1.—Illustration of the geometry used to define the quantities in eqs. (1) and (3). The (X, Y)-plane is the plane of the sky, with the observer looking along the Z-axis. The (X, Y')-plane is the plane of the galaxy, which is tilted by an inclination angle i away from the plane of the sky. The azimuth angle within the plane of the galaxy is given by θ. Each spiral arm segment is interpreted as a portion in azimuth of a rotating cylinder with thickness ΔR and height h at a radius R and rotation velocity V_c.

TABLE 1

VELOCITY GRADIENTS OF SPIRAL ARM SEGMENTS

Y (arcmin) (1)	NORTHERN dV/dX (km s^{-1} arcmin^{-1})									SOUTHERN dV/dX (km s^{-1} arcmin^{-1})						
	o (2)	L (3)	k (4)	H (5)	g (6)	D (7)	c (8)	(9)	(10)	n (11)	K (12)	j (13)	G (14)	f (15)	C (16)	b (17)
31.2	*	...	...	...	...	...	...	...	...	...	...	...	...	...	...	...
30.0	*	...	...	...	...	...	...	...	...	...	...	...	...	...	...	...
28.8	*	...	...	...	...	...	...	...	...	...	...	...	...	...	...	...
27.6	*	...	...	...	...	...	...	...	...	...	...	...	...	...	...	...
26.4	1.42!	...	...	...	...	...	...	...	...	*	...	...	...	...	...	...
25.2	1.35!	...	...	...	...	...	...	...	...	1.47!	...	...	...	...	...	...
24.0	1.36!	...	...	...	...	...	...	...	...	1.62!	...	...	...	...	...	...
22.8	1.47!	*	...	...	...	...	...	...	...	1.74!	...	...	...	...	...	...
21.6	*	2.50	...	...	...	...	...	...	...	1.67!	...	...	...	...	...	...
20.4	...	2.45!	...	...	...	...	...	...	...	1.67	...	...	...	...	...	...
19.2	...	2.55!	...	...	...	...	...	...	...	1.70	2.84!	...	...	...	...	...
18.0	...	2.66!	3.18	...	...	...	...	...	...	1.77	2.82!	...	...	...	...	...
16.8	...	2.52!	3.17	...	...	...	...	...	...	1.71	3.07!	...	...	...	...	...
15.6	...	2.52	3.55	...	...	...	...	...	...	2.02	2.85!	...	...	...	...	...
14.4	...	2.76	3.64	*	...	...	...	...	...	...	2.95!	*	...	...	...	...
13.2	...	2.71	4.12!	4.95	...	...	...	...	...	...	2.95!	*	5.81	...	...	...
12.0	...	2.58	4.10!	5.21!	...	...	...	...	...	...	2.95!	*	5.84	...	...	...
10.8	...	2.44	4.05!	5.29!	...	...	...	...	...	...	3.03	4.77!	6.30	...	...	...
9.6	...	...	4.08!	5.47!	...	...	...	...	...	...	3.07	4.77!	6.37!	...	...	...
8.4	...	...	4.05!	5.75!	...	...	...	...	...	...	2.87	4.58!	6.70!	...	...	...
7.2	...	...	4.03!	6.01!	...	...	...	...	...	...	...	4.58!	6.77!	*	...	...
6.0	...	...	4.03!	*	*	10.22!	...	...	...	...	...	4.83!	6.63	9.59!	14.15!	...
4.8	...	...	3.92	*	*	12.13!	...	...	...	...	...	4.70	...	10.25!	15.67!	...
3.6	...	...	3.85	*	9.52!	16.57!	...	...	...	...	...	*	...	10.67	17.87!	...
2.4	...	...	...	*	8.97!	16.28!	55.76!	...	...	...	...	*	...	...	...	...
1.2	...	...	...	...	8.57	*	52.61	...	...	...	...	...	...	...	...	86.54!
0.0	...	...	...	...	8.42	*	44.10	86.54	...	...	...	...	...	...	19.63	73.14
−1.2	...	...	...	...	9.26	*	38.54!	84.99!	...	...	...	...	7.83	...	18.37	95.25!
−2.4	...	...	...	...	9.22	12.98!	29.85!	...	...	...	...	...	7.83!	...	24.91!	95.25
−3.6	...	...	...	4.93	8.33!	12.93!	27.60!	...	...	...	...	*	8.02!	...	...	...
−4.8	...	...	3.57	4.70	7.37!	10.63!	*	...	...	...	...	6.58	8.16!	11.39!	...	...
−6.0	...	...	3.37!	4.75!	7.48!	...	...	...	...	...	...	6.42!	7.80!	11.55!	...	...
−7.2	...	...	3.43!	4.56!	6.10!	...	...	...	...	3.03	...	5.90!	7.42!	*	...	...
−8.4	...	...	3.64!	4.43!	*	...	...	...	...	3.10	...	5.27!	7.45!	...	...	...
−9.6	...	...	3.73!	4.62!	...	...	...	...	...	2.92	*	5.35!	...	...	...	...
−10.8	...	*	3.66!	4.54!	...	...	...	...	*	2.42!	3.37!	4.43	...	...	...	...
−12.0	...	*	3.43!	4.21	...	...	...	...	*	2.39!	3.38!	...	...	...	...	...
−13.2	...	2.60	3.49!	...	...	...	...	...	*	2.36!	3.42!	...	...	...	...	...
−14.4	...	2.39!	3.50!	...	...	...	...	...	2.14!	*	3.42!	...	...	...	...	...
−15.6	...	2.33!	3.13	...	...	...	...	...	2.19!	*	3.52	...	...	...	...	...
−16.8	...	2.30!	...	...	...	...	...	...	2.16!	*	3.45	...	...	...	...	...
−18.0	...	2.36!	...	...	...	...	...	...	2.19	...	3.38	...	...	...	...	...
−19.2	...	2.23!	...	...	...	...	...	...	2.19	...	3.50	...	...	...	...	...
−20.4	...	2.20!	...	...	...	...	...	...	2.14	...	...	...	...	...	...	...
−21.6	...	2.03!	...	...	...	...	...	...	2.09	...	...	...	...	...	...	...
−22.8	...	1.86	...	...	...	...	...	...	2.20	...	...	...	...	...	...	...
−24.0	...	1.86	...	...	...	...	...	...	2.20	...	...	...	...	...	...	...
−25.2	...	*	...	...	...	...	...	...	*	...	...	...	...	...	...	...
		M	l	I	h	E	d	A	N	m	J	i	F	e	B	a

The columns of Table 1 have been ordered according to increasing gradient for the northern and southern halves of the galaxy. Examination of the table reveals corresponding arm segment pairs with comparable velocity gradients east and west of the major axis. Their correspondence is further clarified by a number of such segments which can be tracked continuously across the major axis. The mean of well-defined velocity gradients is in all cases larger on the far side (positive Y) than on the near side for receding (positive X) arm segments, and vice versa for the approaching arm segments. Furthermore, these arm segment pairs have counterparts on alternating halves of the galaxy with a continuously varying velocity gradient. The columns of Table 1 are headed and followed by letter designations a–o and A–N that indicate the two interleaved series of such arm segments. This pattern is consistent with and suggestive of a global two-arm trailing spiral.

A mean position is also associated with each of the arm segments defined in Table 1. The mean minor-axis coordinate, Y, follows directly from the range of well-determined gradients indicated in the table. The corresponding major-axis coordinate, X, is obtained from the ridgeline seen in those same position velocity images supplemented with the ridge position observed in the integrated hydrogen distribution (Fig. 3*a* of Brinks 1984, Fig. 9 of BS84, Fig. 5 of E74, and Fig. 4 of Braun 1990). These positions, together with the corresponding velocity gradients and their estimated errors, are listed separately for the two apparent spiral arms in Tables 3A and 3B. Also listed are the average velocity offsets for the well-determined

TABLE 2

VELOCITY OFFSETS OF SPIRAL ARM SEGMENTS

Y (arcsec) (1)	SYSTEMIC VELOCITY OFFSETS (km s^{-1}) no (2)	KL (3)	jk (4)	GH (5)	fg (6)	CD (7)	bc (8)	(9)
31.2	...	...	...	...	...	...	...	...
30.0	...	...	...	...	...	...	...	...
28.8	...	...	...	...	...	...	...	...
27.6	...	...	...	...	...	...	...	...
26.4	+20	...	...	...	...	...	...	...
25.2	+20	...	...	...	...	...	...	...
24.0	+20	...	...	...	...	...	...	...
22.8	+20	...	...	...	...	...	...	...
21.6	+15	−5	...	...	...	...	...	...
20.4	+5	−20	...	...	...	...	...	...
19.2	+10	−15	...	...	...	...	...	...
18.0	+10	−10	+20	...	...	...	...	...
16.8	0	0	+20	...	...	...	...	...
15.6	...	0	+10	...	...	...	...	...
14.4	...	+10	+10	...	...	...	...	...
13.2	...	+10	0	0	...	...	...	...
12.0	...	0	0	−5	...	...	...	...
10.8	...	0	0	−5	...	...	...	...
9.6	...	0	+5	−5	...	...	...	...
8.4	...	0	+10	−15	...	...	...	...
7.2	...	...	+10	−10	...	...	...	...
6.0	...	...	0	−10	+10	−10	...	...
4.8	...	...	0	...	0	−30	...	...
3.6	...	...	0	...	0	+10	...	...
2.4	...	...	...	...	0	+25	+65	...
1.2	...	...	...	...	0	...	+25	...
0.0	...	...	...	...	0	0	0	0
−1.2	...	...	...	...	0	0	0	+15
−2.4	...	...	...	...	0	0	0	0
−3.6	...	...	0	+10	+10	+25	+35	...
−4.8	...	...	0	+15	+20	+35	+70	...
−6.0	...	...	+10	+10	+10	+15	+50	...
−7.2	...	...	+10	+10	+10	+10	...	...
−8.4	...	...	+20	+15	0	0	...	...
−9.6	...	...	+20	0	0	−20	...	...
−10.8	...	...	+20	0	0	−20	...	...
−12.0	...	...	+20	+15	...	...	...	...
−13.2	...	+15	+15	+15	...	...	...	...
−14.4	...	+10	+10	+10	...	...	...	...
−15.6	...	+10	+10	+10	...	...	...	...
−16.8	...	+10	+10	...	...	...	...	...
−18.0	...	+10	...	...	...	...	...	...
−19.2	...	+15	...	...	...	...	...	...
−20.4	...	+15	...	...	...	...	...	...
−21.6	...	+20	...	...	...	...	...	...
−22.8	...	+20	...	...	...	...	...	...
−24.0	...	+20	...	...	...	...	...	...
−25.2	...	...	...	...	...	...	...	...
		MN	lm	Ij	hi	EF	de	AB

gradients, as well as the range in minor-axis coordinate, ΔY, over which the arm brightness exceeds 2.5 K and the estimated mean peak brightness in H I. These brightnesses were obtained from Figure 8 of BS84 at a resolution of 60″ spatially and 8.2 km s^{-1} in velocity. The estimated error in the values of ΔY is 1.2, and in the peak arm brightness it is 5 K.

2.2. *Determining Radii of Arm Segments*

The integrated hydrogen distribution (in the above-mentioned figures) also delineates the major-axis crossing point between each of the arm segment pairs. These are particularly important positions, since they allow a direct conversion of angular distance to radius within the galaxy, without the need for an assumed inclination. There is a tendency for the position of the local maximum projected radius of arm segments to be displaced to negative Y on the receding side and positive Y on the approaching side by a few degrees with respect to the nominal major-axis position angle of 38° east of north. Since this departure pattern has both the sense and the approximate magnitude of that expected for a trailing spiral, it seems appropriate to adopt provisionally a fixed major-axis orientation of 38°. The positions of ridgeline crossings of this position angle are indicated in Tables 3A and 3B together with their estimated errors. The width, ΔR, of the arm segments at the major-axis crossings also appears to be a well-defined quantity. Arm segments have relatively flat-topped profiles bounded by steep edges when viewed along the major axis. These widths are also listed in the table.

Each of the major-axis crossing points has been assigned a velocity gradient and estimated error derived from the mean and difference of the measured velocity gradients of the two arm segments which bracket it. The inherent assumption in making this assignment is that the velocity field is locally (i.e., within a $\sim 90°$ interval in local azimuth of the galaxy) axisymmetric. If, for example, the galaxy had a flat rotation curve, $V_c(R)$ = constant, and fixed inclination, the velocity gradient should vary according to $dV/dX \propto 1/R$, a power law of slope -1 in $\ln(dV/dX)$ versus $\ln R$. The actual distribution of $\ln(dV/dX)$ versus $\ln R$ is plotted in Figure 2 with distinct symbols for the two arms. A crude indication for the rotation curve follows directly from the changing slope of this distribution. A relatively flat inner portion is followed by a rapid decline, a slow rise, and a final slow decline. Although the sampling is admittedly sparse, at small radii the two arms are consistent with a single distribution in dV/dX versus R, while at larger radii they show significant departures due to either or both of differing rotation velocities and orientations. This suggests the following approach in assigning radii to the measured values of dV/dX: a piecewise power-law interpolation between *all* the measured major-axis crossings inside a radius of about 20′ ($dV/dX > 12$ km s^{-1} arcmin^{-1}) with a *separate* piecewise power law for each of the two arms beyond this radius ($dV/dX < 12$). The coupled interpolation inside a 20′ radius introduces the further assumption of bisymmetry in the velocity of the inner galaxy. The interpolated radii are listed for the observed arm segments in Table 3, together with their estimated errors. Similarly, the width of arm segments has been interpolated linearly as a function of radius from the locations

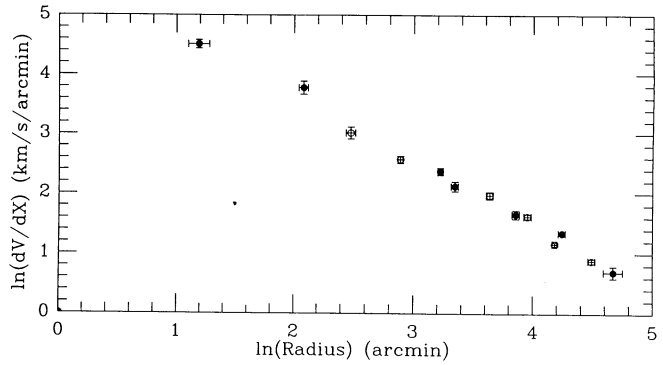

FIG. 2.—Velocity gradients of major-axis crossing points. The data are taken from Table 3, with filled symbols representing positions of arm a–o (Table 3A) and open symbols of arm A–N (Table 3B).

TABLE 3A

PARAMETERS OF SPIRAL ARM SEGMENTS a–o

Segment (1)	$X \pm$ Error (2)	$Y \pm$ Error (3)	dY (4)	$dV/dX \pm$ Error (km s^{-1} arcmin^{-1}) (5)	dV_{sys} (km s^{-1}) (6)	T_p (K) (7)	$R \pm$ Error (8)	dR (9)	$i \pm$ Error (10)	θ (11)	ϕ (12)	$V_c \pm$ Error (km s^{-1}) (13)	$V_e \pm$ Error (14)	h (kpc) (15)	$s_E \pm$ Error (pc) (16)
a	−2.2 ± 0.3	−1.2 ± 0.3	2.4	95.0 ± 10.0	0	2.5	3.1 ± 0.3	1.8	57.1 ± 9.4	−135°	135°	353 ± 63	289 ± 52	0.41	0 ± 0
	−3.3 ± 0.3	0.0 ± 0.3	0.0	91.0 ± 7.0	0	0.0	3.3 ± 0.3	1.8	58.6 ± 0.0	180	180	0 ± 0	0 ± 0	0.00	0 ± 0
b	−2.5 ± 0.3	1.2 ± 0.3	2.4	87.0 ± 10.0	25	2.0	3.5 ± 0.3	1.8	60.1 ± 8.3	136	224	348 ± 58	285 ± 48	0.41	0 ± 0
c	1.4 ± 0.3	2.4 ± 0.3	2.4	56.0 ± 5.0	65	3.5	5.9 ± 0.4	2.0	65.4 ± 3.3	76	284	366 ± 42	300 ± 34	0.35	0 ± 0
	8.0 ± 0.5	0.0 ± 0.3	0.0	44.0 ± 5.0	0	0.0	8.0 ± 0.5	2.1	63.9 ± 0.0	0	360	0 ± 0	0 ± 0	0.00	0 ± 0
d	7.9 ± 0.3	−2.4 ± 0.3	4.8	32.0 ± 4.0	18	5.0	9.4 ± 0.5	2.6	62.4 ± 3.8	−33	393	341 ± 48	280 ± 39	0.93	0 ± 0
e	−5.8 ± 0.3	−5.4 ± 0.3	3.6	11.5 ± 1.0	60	15.0	22.1 ± 0.5	4.0	75.4 ± 1.5	−105	465	263 ± 24	263 ± 24	0.54	151 ± 72
	−25.0 ± 0.5	0.0 ± 0.3	0.0	10.7 ± 0.7	0	0.0	25.0 ± 0.5	4.2	75.0 ± 0.0	180	540	0 ± 0	0 ± 0	0.00	0 ± 0
f	16.4 ± 0.3	5.4 ± 0.3	4.8	9.9 ± 1.0	5	15.0	26.0 ± 0.5	4.8	74.5 ± 1.6	129	591	267 ± 28	267 ± 28	0.79	220 ± 76
g	24.1 ± 0.3	3.0 ± 0.3	7.2	9.3 ± 1.0	0	15.0	26.8 ± 1.0	5.2	75.1 ± 1.5	26	694	258 ± 29	258 ± 29	1.37	382 ± 92
	28.2 ± 1.0	0.0 ± 0.3	0.0	8.3 ± 0.7	0	0.0	28.3 ± 1.0	6.1	74.4 ± 0.0	0	720	0 ± 0	0 ± 0	0.00	0 ± 0
h	26.3 ± 0.5	−5.4 ± 0.3	7.2	7.3 ± 0.8	13	15.0	32.6 ± 1.0	6.2	73.7 ± 1.7	−36	756	248 ± 28	248 ± 28	1.29	359 ± 90
i	−30.8 ± 0.5	−7.8 ± 0.6	8.4	5.7 ± 0.5	5	15.0	42.6 ± 1.5	6.5	74.6 ± 1.6	−136	856	252 ± 24	252 ± 24	1.50	417 ± 97
	−47.1 ± 1.5	0.0 ± 0.6	0.0	5.2 ± 0.4	0	0.0	47.1 ± 1.5	6.6	75.2 ± 0.0	180	900	0 ± 0	0 ± 0	0.00	0 ± 0
j	−41.1 ± 0.5	8.4 ± 0.6	13.2	4.7 ± 0.3	5	50.0	53.5 ± 1.5	7.6	75.8 ± 1.5	140	940	259 ± 18	259 ± 18	2.48	413 ± 45
k	36.3 ± 0.5	9.8 ± 0.6	15.6	4.1 ± 0.2	4	50.0	63.5 ± 2.0	9.2	79.4 ± 1.1	55	1025	265 ± 15	265 ± 15	2.89	483 ± 47
	69.3 ± 2.5	0.0 ± 1.0	0.0	3.8 ± 0.1	0	0.0	69.8 ± 2.5	10.2	79.9 ± 0.0	0	1080	0 ± 0	0 ± 0	0.00	0 ± 0
l	41.7 ± 0.5	−10.2 ± 0.6	12.0	3.5 ± 0.2	14	45.0	73.5 ± 3.0	10.5	80.3 ± 1.0	−55	1135	261 ± 18	261 ± 18	2.14	370 ± 46
m	−46.0 ± 5.0	−12.0 ± 0.6	10.8	2.4 ± 0.1	18	20.0	94.4 ± 5.0	12.7	81.6 ± 0.8	−119	1199	229 ± 15	229 ± 15	1.86	446 ± 80
	−107.0 ± 8.0	0.0 ± 1.0	0.0	2.0 ± 0.2	0	0.0	106.5 ± 8.0	13.9	79.7 ± 0.0	180	1260	0 ± 0	0 ± 0	0.00	0 ± 0
n	−52.8 ± 0.8	23.4 ± 1.0	12.0	1.6 ± 0.1	19	15.0	123.4 ± 8.0	15.7	77.9 ± 1.2	115	1325	202 ± 18	202 ± 18	1.85	515 ± 109
o	45.0 ± 3.0	24.6 ± 1.0	10.8	1.4 ± 0.1	20	10.0	134.8 ± 8.0	16.9	78.8 ± 1.1	70	1370	192 ± 18	192 ± 18	1.57	567 ± 166

TABLE 3B

PARAMETERS OF SPIRAL ARM SEGMENTS A–N

Segment (1)	$X \pm$ Error (2)	$Y \pm$ Error (3)	dY (4)	$dV/dX \pm$ Error (km s^{-1} arcmin^{-1}) (5)	dV_{sys} (km s^{-1}) (6)	T_p (K) (7)	$R \pm$ Error (8)	dR (9)	$i \pm$ Error (10)	θ (11)	ϕ (12)	$V_c \pm$ Error (km s^{-1}) (13)	$V_e \pm$ Error (km s^{-1}) (14)	h (kpc) (15)	$s_E \pm$ Error (pc) (16)
A	2.6 ± 0.3	−1.2 ± 0.3	2.4	85.0 ± 10.0	15	2.0	3.6 ± 0.3	1.8	60.6 ± 8.1	−43°	223°	348 ± 57	285 ± 47	0.41	0 ± 0
B	−6.6 ± 0.3	−2.4 ± 0.3	2.4	24.9 ± 3.0	0	2.5	10.8 ± 0.5	3.1	73.6 ± 2.1	−128	308	280 ± 36	280 ± 36	0.36	0 ± 0
	−12.0 ± 0.5	0.0 ± 0.3	0.0	20.4 ± 2.0	0	0.0	12.0 ± 0.5	3.6	71.5 ± 0.0	180	360	0 ± 0	0 ± 0	0.00	0 ± 0
C	−6.4 ± 0.3	4.8 ± 0.3	3.6	15.9 ± 1.5	−10	5.0	15.0 ± 0.5	3.6	69.4 ± 2.2	115	425	256 ± 26	256 ± 26	0.52	0 ± 0
D	5.9 ± 0.3	5.2 ± 0.3	4.8	13.8 ± 1.5	−1	10.0	17.1 ± 0.5	3.6	71.1 ± 2.0	70	470	250 ± 28	250 ± 28	0.76	283 ± 112
	17.9 ± 0.5	0.0 ± 0.3	0.0	13.0 ± 0.8	0	0.0	18.1 ± 0.5	3.6	72.6 ± 0.0	0	540	0 ± 0	0 ± 0	0.00	0 ± 0
E	14.5 ± 0.3	−3.6 ± 0.3	3.6	12.2 ± 1.0	20	10.0	19.6 ± 0.5	3.7	74.1 ± 1.6	−42	582	248 ± 21	248 ± 21	0.61	219 ± 102
F	−29.0 ± 0.6	−5.4 ± 0.6	8.4	7.8 ± 0.6	14	30.0	34.0 ± 1.0	4.6	72.3 ± 2.0	−149	689	278 ± 23	278 ± 23	1.61	324 ± 55
	−37.8 ± 1.0	0.0 ± 0.6	0.0	7.2 ± 0.4	0	0.0	37.5 ± 1.0	4.8	75.0 ± 0.0	180	720	0 ± 0	0 ± 0	0.00	0 ± 0
G	−11.2 ± 0.6	8.4 ± 0.6	8.4	6.6 ± 0.4	−10	35.0	40.7 ± 1.0	5.5	77.6 ± 1.3	106	794	275 ± 18	275 ± 18	1.49	284 ± 50
H	31.4 ± 0.6	9.6 ± 0.6	10.8	5.6 ± 0.3	−8	50.0	47.3 ± 1.5	7.2	74.2 ± 1.6	48	852	275 ± 17	275 ± 17	1.94	324 ± 43
	52.0 ± 1.5	0.0 ± 0.6	0.0	5.1 ± 0.2	0	0.0	51.5 ± 1.5	8.3	75.9 ± 0.0	0	900	0 ± 0	0 ± 0	0.00	0 ± 0
I	36.3 ± 0.6	−8.4 ± 0.6	9.6	4.6 ± 0.2	7	45.0	54.4 ± 1.5	9.3	78.0 ± 1.2	−48	948	256 ± 13	256 ± 13	1.67	289 ± 45
J	−10.6 ± 0.6	−12.6 ± 0.6	10.8	3.4 ± 0.1	10	35.0	63.3 ± 1.5	12.4	78.4 ± 1.2	−100	1000	220 ± 8	220 ± 8	1.70	323 ± 51
	−65.1 ± 1.5	0.0 ± 1.2	0.0	3.2 ± 0.1	0	0.0	65.3 ± 1.5	13.1	77.7 ± 0.0	180	1080	0 ± 0	0 ± 0	0.00	0 ± 0
K	−41.1 ± 0.6	13.6 ± 0.6	12.0	2.9 ± 0.1	−1	30.0	72.6 ± 1.5	13.2	76.9 ± 1.3	124	1136	216 ± 9	216 ± 9	1.96	394 ± 58
L	44.1 ± 0.6	18.6 ± 0.6	13.2	2.6 ± 0.1	−11	25.0	82.0 ± 2.0	13.5	74.4 ± 1.6	57	1203	221 ± 10	221 ± 10	2.11	457 ± 69
	89.0 ± 2.5	0.0 ± 1.5	0.0	2.4 ± 0.1	0	0.0	89.6 ± 2.5	13.7	76.7 ± 0.0	0	1260	0 ± 0	0 ± 0	0.00	0 ± 0
M	8.8 ± 0.6	−18.0 ± 0.6	14.4	2.3 ± 0.1	13	20.0	93.9 ± 2.5	13.8	78.9 ± 1.1	−85	1345	220 ± 11	220 ± 11	2.40	576 ± 92
N	−35.0 ± 3.0	−15.6 ± 0.6	14.4	2.2 ± 0.1	10	20.0	98.6 ± 2.5	14.0	80.3 ± 1.0	−111	1371	220 ± 11	220 ± 11	2.47	595 ± 94

of major-axis crossings to the intermediate measurement positions.

2.3. *Determining Further Parameters*

Having established radii for each of the arm segments, the local inclination can be calculated by comparing the projected and actual radius from

$$i = \cos^{-1}\left(\frac{Y^2}{R^2 - X^2}\right)^{1/2}. \quad (4)$$

Although the best precision should be obtained near the minor axis (where $R^2 - X^2$ is large), this is where the errors in Y become largest due to the difficulty of disentangling overlapping features along the line of sight. The intermediate positions where the measurements of arm segments have been made are probably close to the minimum in this system of conflicting error contributions. Inclinations with their estimated errors are listed in Table 3 and plotted in Figure 3. The inclination varies significantly within the range 70°–80° between about 10′ and 140′ radius. Between 10′ and 60′ radius, these variations are well correlated in the two arms, while between 60′ and 100′ the variations appear to uncouple. Inside 10′ there is a rapid drop to an implied inclination of about 55°. Although this may to some extent be a consequence of the assumption of local axisymmetry of the velocity field, it seems likely for the most part to represent a real variation in the disk orientation.

Having determined the local inclination, the rotation velocity follows directly from equation (2), the position angle θ in the local disk plane from

$$\theta = \tan^{-1}\left(\frac{Y}{X \cos i}\right), \quad (5)$$

and the thickness of the gaseous disk as measured to a surface brightness of 2.5 K from equation (3). These quantities are listed in Table 3, together with the cumulated azimuth, $\phi = -\theta + 2n\pi$, along each spiral arm. Assuming that the correct sequence of spiral arm segments has been identified, the three-dimensional distribution and kinematics of the gas are now completely parameterized.

3. SPIRAL STRUCTURE

As discussed in § 2, the two continuous sequences in position and velocity gradient of measured arm segments listed in Table 1 are strongly indicative of a global two-arm trailing spiral pattern which is fully parameterized, under the assumption of local axisymmetry (over ~90° of azimuth) and bisymmetry (inside a 20′ radius) in the gas orbits, by the positions and velocities listed in Table 3. In this section we will first address the question of continuity of these features into a global pattern and then consider some of the consequences of this interpretation.

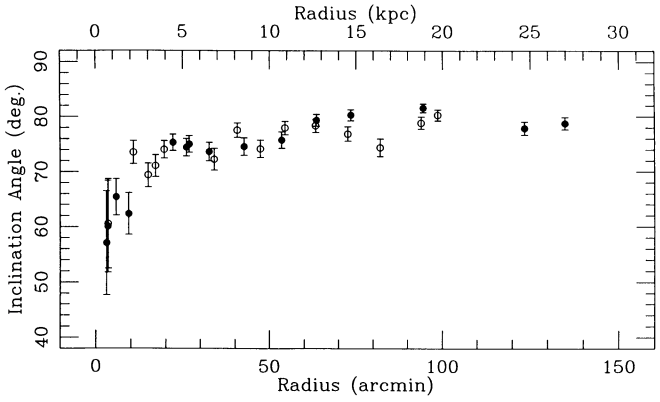

FIG. 3.—Local inclination of spiral arm segments. The inclination from face-on at each of the arm segment positions listed in Table 3 is plotted with respect to a major-axis orientation of 38° east of north. Closed and open symbols correspond to arms a–o and A–N, respectively.

3.1. *Continuity of Spiral Structure*

The coordinates and velocities of Table 3 have been interpolated at 2°.5 intervals in local cumulated azimuth ϕ, using the following piecewise interpolation functions: an exponential of ϕ for the radius, a power law of radius for the velocity gradient dV/dX, and a linear dependence of inclination and velocity offset on ϕ. Functional forms from the last measured interval were used to extrapolate values for an additional 45° in azimuth.

The projected distribution on the sky in major- and minor-axis coordinates is shown in Figure 4, together with the measurement points of Table 3. The rather coarse scale of Figure 4*a* is intended to allow comparison with the large-scale distribution of integrated hydrogen (Fig. 5 of E74). The intermediate and fine scales shown in Figures 4*b* and 4*c* can be compared with the appropriate references (Fig. 9 of BS84, Fig. 14*a* of Walterbos & Kennicutt 1988, Fig. 3*a* of Brinks 1984, and Figs. 3 and 4 of Ciardullo et al. 1988), taking care to obtain the correct orientation (northeast is $+X$, $+Y$). The catalog of 981 Hα nebulae of Pellet et al. (1978) has been overlaid on Figure 4*b* to illustrate the generally good correspondence of neutral and ionized gas tracers of the spiral structure. While the measured points indicated in Figure 4 correspond by definition to ridgelines in integrated H I, the interpolated segments joining them can be seen to delineate the system of arm segments seen in projection in most cases. Departures of the interpolated ridgelines from those seen in integrated H I are usually less than 1′. Correspondence with the dust lanes emphasized in the unsharp-masked exposure of Walterbos & Kennicutt (1988) is also particularly striking. This extends to the inner galaxy (Fig. 4*c*), where the correspondence with the emission line and dust arms illustrated in Ciardullo et al. (1988) can be seen (especially near $X = -3'$).

Although departures from the interpolated arm pattern are generally small, one region in particular deserves special mention. All available tracers near the region $(X, Y) = (+20', -10')$ are displaced to negative Y from the interpolated arm segment by about 2′. The interpolation function is clearly inappropriate in this interval and has therefore been represented with a broken line. Other departures from a "clean" pattern, in the form of a number of apparent interarm connections, can be seen, for example, in the overlaid distribution of Hα in Figure 4*b* at $(X, Y) = (-40', 0')$ and $(-55', +5')$. Despite these departures, the two trailing arms provide a rather complete description of the projected distribution of neutral gas.

The projected distribution in line-of-sight velocity against major-axis coordinate X is shown in Figure 5 for the interpolated data base. All minor-axis coordinates Y have been collapsed into this single position-velocity diagram. The crowding of individual points (spaced by 2°.5 in local azimuth) gives an indication of expected relative brightness for an otherwise uniform gas distribution along the arms. A finite arm width will translate into a flaring ($\Delta X = \Delta R \cos \phi$) at the extreme velocity end of each loop. For a given range in Y, only

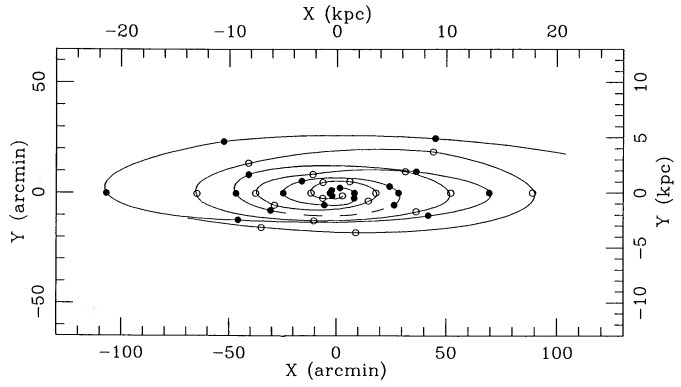

FIG. 4*a*

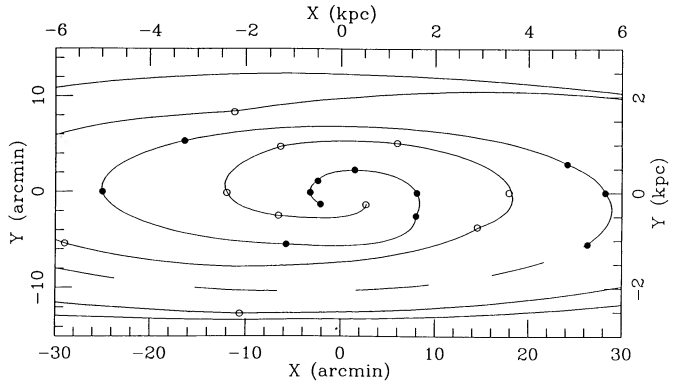

FIG. 4*c*

FIG. 4.—Projected distribution of spiral arms. The measured positions of Table 3 are plotted with closed and open symbols corresponding to arms a–o and A–N, respectively. The solid lines are interpolated values as described in § 3.1. (*a*) Complete distribution at a coarse scale. (*b*) Intermediate-scale structure at an expanded scale with the Hα nebulae from the catalog of Pellet et al. (1978) superposed. (*c*) Structure in the inner galaxy at a further expanded scale. The poorly interpolated segment near $Y = -10'$ is indicated by a broken line.

a portion of this distribution will be seen, as in the series of such images (Fig. 8 of BS84) from which this parameterization was derived. Comparison with this series shows the good correspondence of quasi-linear features with loop segments in Figure 5.

3.2. *Implications of Spiral Structure*

Having gained confidence in the appropriateness of a global two-arm trailing spiral in describing the distribution of gas in M31, it is worth considering the physical consequences of this interpretation. A good impression of the overall structure is given in Figure 6, where the interpolated and measured positions have been rectified to give a face-on view of the galaxy. Due to the continuously varying inclination, this distribution is not related in the usual straightforward fashion to the projected distribution shown in Figure 4. At radii less than about 25′, the pattern is somewhat irregular and elliptical in appearance, most obviously near $X = -10'$, $Y' = -20'$. At intermediate radii the two arms are reasonably symmetric and well separated. At radii larger than about 80′ the two arms begin to merge into a single structure.

Another view of this structure is given in Figure 7, where values of ln R for the arm segments listed in Table 3 are plotted against the cumulated azimuth ϕ, corresponding to the pattern phase. Perfectly logarithmic spirals will be linear in such a plot.

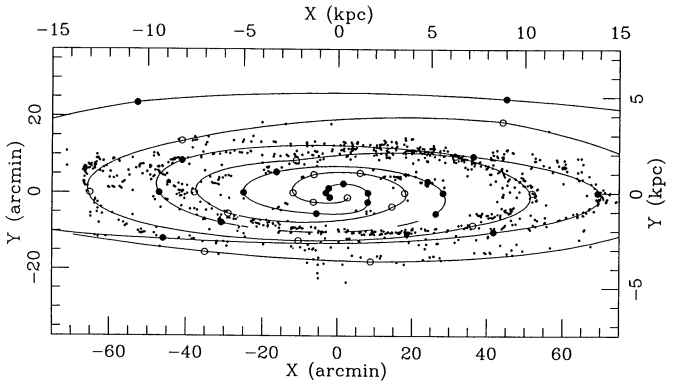

FIG. 4*b*

Three crudely defined regions seem to be indicated for the mean behavior of the two spiral arms: (1) a steep, semilinear but irregular rise from $0° < \phi_1 < 600°$, $1.0 < \ln R_1 < 3.3$, (2) a more shallow linear rise from $600° < \phi_2 < 1150°$, $3.3 < \ln R_2 < 4.4$, and (3) a final divergence of the two arms beyond $\phi_3 > 1150°$, $\ln R_3 > 4.4$. The location of the transition between regions 2 and 3 is somewhat difficult to identify, although the last three filled circles in the figure should arguably appear at a 360° higher phase, since they already represent the merged arm structure seen in Figure 6. Bearing this in mind allows definition of this second transition with some confidence. Linear regression solutions for the two inner regions averaging over both arms give

$$R_1 = 1.'5(\pm 0.'1) \exp\,[0.0050(\pm 0.0002)\phi_1]\,, \quad (6)$$

$$R_2 = 7.'5(\pm 1.'2) \exp\,[0.00205(\pm 0.00015)\phi_2]\,. \quad (7)$$

The corresponding pitch angles are $\psi_1 = 16°$ and $\psi_2 = 6.°7$. The pitch angle for region 2 is similar to that estimated by Arp

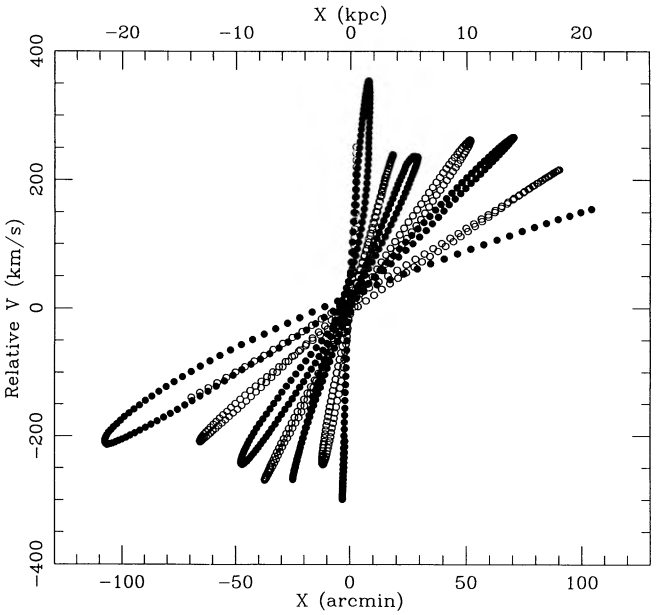

FIG. 5.—Projected distribution of line-of-sight velocity with major-axis coordinate X. The interpolated data base, at 2.°5 intervals in local azimuth, is represented by closed and open symbols for arms a–o and A–N, respectively. All minor-axis coordinates Y have been collapsed into this single position-velocity diagram to allow convenient comparison with the individual diagrams in the literature.

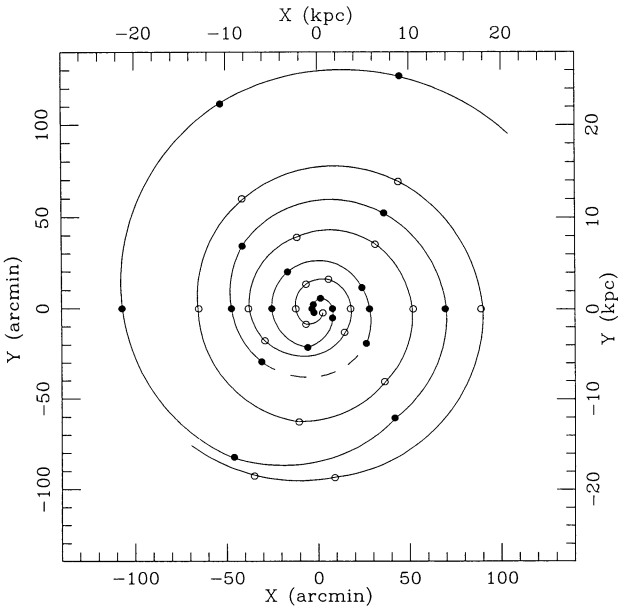

FIG. 6.—Face-on rectified distribution of spiral arms. Measurement points from Table 3 are indicated with closed and open symbols for arms a–o and A–N, respectively. The solid lines are the interpolated values as described in § 3.1. Since the inclination is continuously varying, this distribution is not related in the usual simple fashion to that shown in Fig. 4. The poorly interpolated segment near $Y = -30'$ is indicated with a broken line.

(1964), $\psi = 7°.4$, from the major-axis crossings of optical arm tracers identified by Baade (1963). Comparing Figures 6 and 7 illustrates the correspondence of these three regions: the irregular elliptical pattern in the inner galaxy, the well-developed symmetric logarithmic spiral at intermediate radii, and the final dissolution of spiral structure in the outer galaxy.

The velocity offsets listed in Table 2 give a direct indication for the prevalence and magnitude of shocks in the spiral arms, as smoothed in the data base ($1' = 200$ pc along X) within

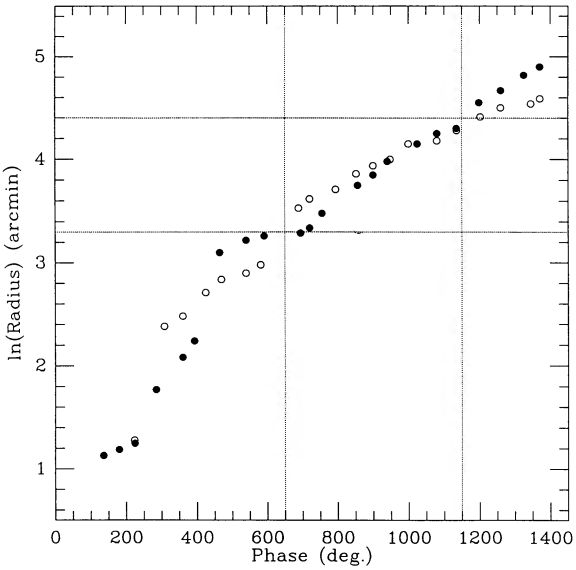

FIG. 7.—Relationship between radius and pattern phase. The measurement points of Table 3 are indicated with closed and open symbols for arms a–o and A–N, respectively. The dotted lines indicate the three apparent regimes of radius discussed in the text.

which they were measured. The clearest signature of a shock is the occurrence of significantly different offsets across an individual arm, corresponding to the detection of both preshock and postshock gas (e.g., Visser 1980), in contrast to a general shift for the complete arm. A systematic variation in the gradient of velocity offsets across individual arms, $d(\Delta V_{sys})/dY$, is observed as a function of radius in Table 2. Large gradients of the offsets can be seen in the inner galaxy at radii between 4′ and 25′, where the gradients are typically 40 km s^{-1} across the arms. At intermediate radii, between 30′ and 75′, there are gradients of about 20 km s^{-1} across the arms, while for radii greater than 85′ the gradients are less than about 10 km s^{-1}. Local minima in the gradient of velocity offset occur at radii near 25′ and 80′, where the velocity offsets themselves disappear. Once again, distinctive properties are found for the three regimes of radius identified above.

4. ROTATION CURVE AND MASS DISTRIBUTION

Interpretation of the rotation velocities derived in § 2.3 and listed in Table 3 requires an assumption about the axisymmetry of the velocity field. If we assume that gas orbits are purely circular, these velocities can be used directly to define a rotation curve and the underlying mass distribution. If, on the other hand, there are significant azimuthal perturbations of the velocity field, it will first be necessary to extract, if possible, the axisymmetric component. Since there are a number of indications for ellipticity in the inner galaxy, we will consider both of these assumptions in turn.

4.1. *Circular Gas Orbits*

Assuming for the moment only circular gas motions, we obtain the rotation curve plotted in Figure 8*a*. At an assumed distance of 690 kpc (e.g., Baade & Swope 1963), 1′ corresponds to 200 pc. Rotation velocities of about 350 km s^{-1} are implied inside about 2 kpc, followed by a relatively constant 260 km s^{-1} out to 10 kpc and a subsequent decline to 200 km s^{-1} by a radius of 26 kpc. The two arms give consistent rotation velocities, except in the range 12–16 kpc, where they are separated by about 40 km s^{-1}. A comparably large and significant departure is seen over the same range in radius in the nebular spectroscopy of Rubin & Ford (1970, hereafter RF70). The high velocity peak in the inner galaxy is quite remarkable in relation to previously observed rotation curves (e.g., Kormendy & Norman 1979), although the physical resolution and sensitivity obtained for M31 allow probing of a region not generally accessible to study.

Also shown in Figure 8*a* is the best-fit rotation curve obtained with a spheroidal bulge, exponential stellar disk, gaseous disk, and central compact mass. The effective radius of the bulge, $r_e = 2.0$ kpc, and scale length of the stellar disk, $r_s = 5.8$ kpc, were taken from Walterbos & Kennicutt (1988). The radial distribution of neutral hydrogen gas density along the major axis and total H I mass, $M_{\rm H\,I} = 4 \times 10^9\ M_\odot$, were taken from E74 and Cram et al. (1980). A total gas mass $M_G = 1.5\ M_{\rm H\,I}$ was estimated on the basis of a 10% He contribution and a modest molecular component. It will be seen below that the gas mass is only about 3% of the implied total mass, so that further refinements of this estimate are not essential here. The shape of the resulting rotation curve is determined by the square root of the quadratic sum of the component contributions to rotation velocity. The gaseous disk mass was held fixed in the fitting process, while the masses of the other components were interactively adjusted to minimize the fit residuals using

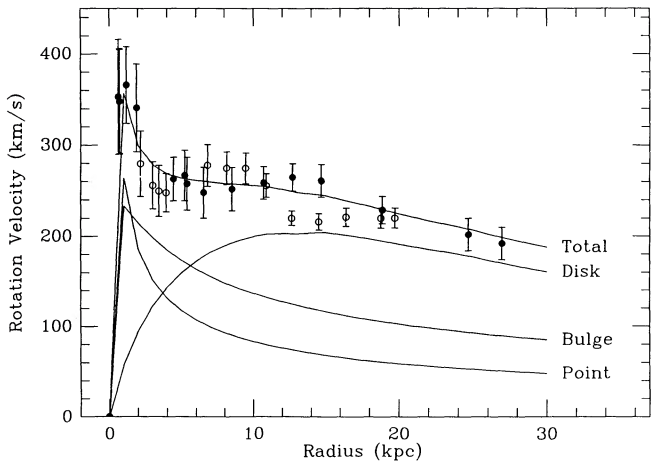

FIG. 8*a*

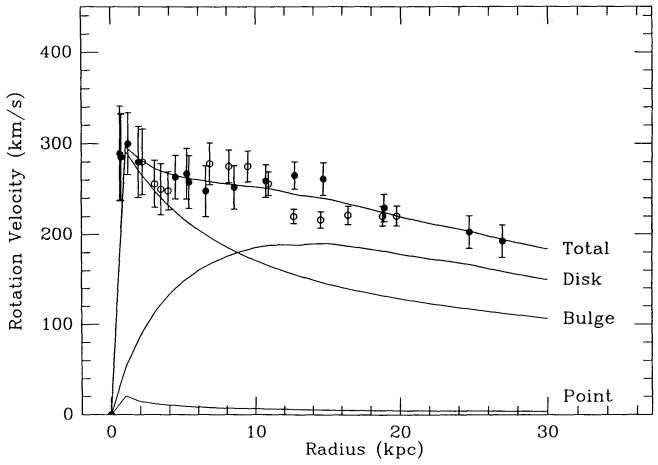

FIG. 8*b*

FIG. 8.—Rotation velocity as a function of radius. The measurement points of Table 3 are indicated with closed and open symbols for arms a–o and A–N, respectively. Solid curves correspond to component contributions and total rotation velocities as indicated, for the results of an interactive fit to the data. (*a*) Rotation curve and fit assuming circular gas orbits, so that derived tangential velocities correspond directly to unperturbed rotation velocities. (*b*) Rotation curve and fit after a 20% correction to tangential velocities inside 2 kpc to account for the observed ellipticity of the spiral structure as described in § 4.2.

the GIPSY task ROTMAS. Since neither bulge nor the disk components were sufficiently centrally peaked to allow fitting of the velocity peak inside 2 kpc (as illustrated by the component rotation velocities also plotted in the figure), it was necessary to introduce a more centrally condensed mass to fit this feature. There are a number of other indications for a more centrally condensed component within M31. A compact nuclear component concentrated within the central arcsecond was first recognized by Light et al. (1974). It has been suggested (Dressler & Richstone 1988; Kormendy 1988) that a 10^7–10^8 $M_\odot$ black hole may lurk within this region. However, even with the inclusion of this compact component, the fit in the central region is not very satisfactory. The component masses of the fit shown in Figure 8*a* are listed in Table 4. In particular, the compact mass, $M_N = 1.6 \times 10^{10}$ $M_\odot$, is uncomfortably large. Such a mass concentration should lead to a much more obvious kinematic signature in the stellar velocity dispersions than that observed by Dressler & Richstone (1988) and Kormendy (1988). Mass-to-luminosity ratios for the various components are also listed in Table 4, using the total B luminosities for the bulge, $L_B = 1.2 \times 10^{10}$ $L_\odot$, and for the disk, $L_D = 1.9 \times 10^{10}$ $L_\odot$, given by Walterbos & Kennicutt (1988), and the total V luminosity for the nucleus, $L_N = 5.5 \times 10^6$ $L_\odot$, from Light et al. (1974). While the ratios derived for the bulge and disk are in themselves reasonable, 4.2 and 7.4 $M_\odot/L_\odot$, respectively (cf. Fig. 6 of Kormendy 1988), it is perhaps surprising that this ratio should be lower for the bulge than for the disk. On the other hand, examination of previous mass decompositions in the literature (e.g., Kent 1987; Begeman 1987) consistently shows a trend for finding higher M/L in disks than in bulges. This is a rather curious result, which seems to imply either a systematic error in the decomposition analyses or a very significant property of spiral galaxy bulges. Given the difficulties in interpretation which result from the assumption of purely circular gas orbits, it seems unlikely that this is the correct approach.

4.2. *Elliptical Gas Orbits*

As stated in § 1, there are indications, from the twisting of optical isophotes, for a barlike triaxial ellipsoidal bulge within M31. The most likely parameters of the bulge (Stark 1977) are an axial ratio $n = 1.7 \pm 0.1$ in the mean disk plane and a long-axis orientation of $\theta = -120° \pm 15°$ from the nominal major-axis position angle of 38° east of north. Gasdynamical calculations (e.g., Sanders & Huntley 1976; Mulder 1986) suggest that the gas orbits in the presence of such a potential will be approximately elliptical with the same orientation as the bar and that this perturbation will be primarily confined to the vicinity of the inner Lindblad resonance. The ellipticity of the gas spiral structure in the inner galaxy is confirmed in the current study. As seen in the recitified view of the galaxy in Figure 6, the inner spiral has an elliptical distortion which leads to crowding of the spiral arms, aligned along $\theta = -115° \pm 15°$, (i.e., within about 30° of the line of sight). An axial ratio of $n = 1.9 \pm 0.1$ is suggested by the figure defined by the inner $\pm 10'$ in X and the inner $\pm 20'$ in rectified Y. From Figures 6 and 7 it is clear that the elliptical distortion disappears beyond abut 15′ (i.e., 3 kpc).

When viewing an elliptical orbit nearly along its long axis, the observed velocity for gas near the short axis is related to

TABLE 4

COMPONENT MASS AND MASS-TO-LUMINOSITY RATIOS

Orbit Type (1)	Disk Mass (10^9 $M_\odot$) (2)	Bulge Mass (10^9 $M_\odot$) (3)	Nuclear Mass (10^9 $M_\odot$) (4)	Total Mass (10^9 $M_\odot$) (5)	Disk $M_\odot/L_\odot$ (6)	Bulge $M_\odot/L_\odot$ (7)	Nuclear $M_\odot/L_\odot$ (8)
Circular	141 ± 5	50 ± 5	16 ± 3	207 ± 8	7.4 ± 0.4	4.2 ± 0.4	2950 ± 550
Elliptical	122 ± 5	78 ± 5	0.1[a]	200 ± 7	6.4 ± 0.4	6.5 ± 0.4	18[a]

[a] Assumed value. Not constrained by current data.

the circular velocity at that radius due to the same mass by

$$V_e = V_c\left(\frac{2n-1}{n}\right)^{1/2} \quad (8)$$

for an axial ratio n. This implies that unperturbed rotation velocities will be overestimated by the factor in the square root if circular orbits are assumed. For an axial ratio of 1.9 this amounts to a 20% overestimate of the unperturbed rotation velocity. The velocities in Table 3 have been corrected for ellipticity by assuming a fixed axial ratio $n = 1.9$ inside 2 kpc. The resulting rotation curve is plotted in Figure 8*b*, together with the best-fit rotation curve as before. The central velocity peak noted in the previous subsection has disappeared with the ellipticity corrections, and with it the need to invoke a massive compact component. The quality of fit in the inner galaxy has improved, and the mass-to-luminosity ratios listed in Table 3 are now consistent with a fixed ratio for both the bulge and the stellar disk, $M/L = 6.5\ M_\odot/L_\odot$.

Another noteworthy aspect of the rotation curve is the absence of any need to invoke a massive dark halo component. Between 20 and 28 kpc the rotation velocity is falling at a roughly Keplerian rate. It is certainly possible that a flattening or even an increase in rotation velocity occurs beyond this radius, but it will require a substantial effort to detect more distant gas.

The total implied mass, $(2.0 \pm 0.1) \times 10^{11}\ M_\odot$, is comparable to that reported previously (e.g., RF70). However, it should be stressed that this is the first attempt to solve simultaneously for the three-dimensional gas distribution, and the inclusion of the derived departures from planar and circular symmetry leads to significant differences in the implied rotation curve. In particular, there is no evidence for the deep apparent minimum in rotation velocity at about 2 kpc noted in RF70.

5. DISCUSSION

5.1. *Resonances and Density Waves*

The three regimes in radius discussed in § 3.2 seem to correspond with those predicted by both theoretical and computational studies of spiral structure (e.g., Lin, Yuan, & Shu 1969; Shu, Milone, & Roberts 1973; Toomre 1977) if we identify the boundaries between the inner regions (regions 1 and 2 defined in § 3.2) with the inner Lindblad resonance (ILR), and between the outer regions (regions 2 and 3) with the radius of corotation (CR). Well-developed spiral structure is only expected between the ILR and CR, where the spiral mode can propagate and is accompanied by a strong shock. The gradients of velocity offset discussed in § 3.2 also support the view that shocks are damped at these boundaries and are only organized interior to each of regions 1–3. The implied shock speeds (detected with 1′ resolution) within these regions are 40, 20, and 10 km s^{-1}, respectively. The low value exterior to CR is likely to be transonic and thus only lead to moderate compression. Multiple reflected shocks might be expected in the vicinity of the ILR.

The rotation curve fit to the data in Figure 8*b* can be used to determine the parameters relevant to the disk dynamics: the angular frequency, $\Omega = V/R$, and the epicyclic frequency,

$$\kappa = \left[\frac{2V}{R}\left(\frac{V}{R} + \frac{dV}{dR}\right)\right]^{1/2}, \quad (9)$$

in a form taken from Mihalas & Routly (1968). The primary resonances are (1) the ILR, where the pattern frequency $\Omega_p = \Omega - \kappa/2$; (2) CR, where $\Omega_p = \Omega$; and (3) the outer Lindblad resonance (OLR), where $\Omega_p = \Omega + \kappa/2$. These frequencies are plotted against radius in Figure 9. The boundaries of § 3.2, corresponding to radii of 5.4 and 16.3 kpc, give an indication of the pattern frequency, $\Omega_p = 15 \pm 2$ km s^{-1} kpc^{-1}. This pattern frequency, together with the $\Omega + \kappa/2$ curve in Figure 9, suggests that the OLR should occur at about 22 kpc, the radius at which the two spiral arms begin to merge in Figure 6. There are, thus, a number of morphological and kinematic indications that such an interpretation may be appropriate.

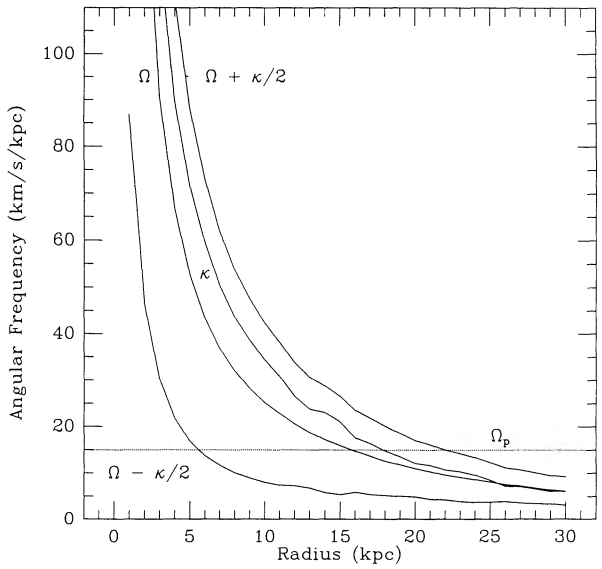

FIG. 9.—Intrinsic frequencies and resonances of the gaseous disk. The angular and epicyclic frequencies which follow from the rotation curve of Fig. 8*b* are plotted together with the inner and outer Lindblad resonances as solid lines. The pattern frequency which follows from the divisions indicated in Fig. 7 is plotted as a dotted line.

5.2. *Drivers of Spiral Structure and Midplane Distortions*

Given the rather clean, grand design spiral pattern derived for M31 in the current study and illustrated in Figure 6, it is natural to consider what the driving force for this pattern might be. At least two possibilities are immediately apparent. The first is the barlike triaxial bulge which is indicated by both the optical isophote twisting (Stark 1977; Hodge & Kennicutt 1982) and the coaligned elliptical distortion of the gas found here. The bulge mass, $8 \times 10^{10}\ M_\odot$, and axial ratio ~ 1.7 should be more than sufficient to drive the observed spiral structure in view of recent gasdynamical calculations (e.g., Mulder 1986). The second likely driver is the nearby companion M32 with a mass of $\sim 3 \times 10^9\ M_\odot$ and an orbit which may extend between about 5 and 16 kpc from M31's nucleus (Byrd 1976).

The substantial departures from a planar gas distribution, indicated in Figure 3 and illustrated directly and in exaggerated form in Figure 10, are most easily understood in terms of a significantly nonplanar mass asymmetry. In the inner galaxy, the midplane is confined to within a few 100 pc of the mean plane, while at large radii the projected midplane extends to a width of more than 1 kpc. The most obvious candidate for such effects is the action of M32, as pointed out by Roberts (1966) and Byrd (1976, 1978). This type of wandering gravitational perturbation may also provide the explanation for the significantly discrepant rotation velocities seen in the two spiral arms in Figure 8 between 12 and 16 kpc radius, especially if, as Byrd

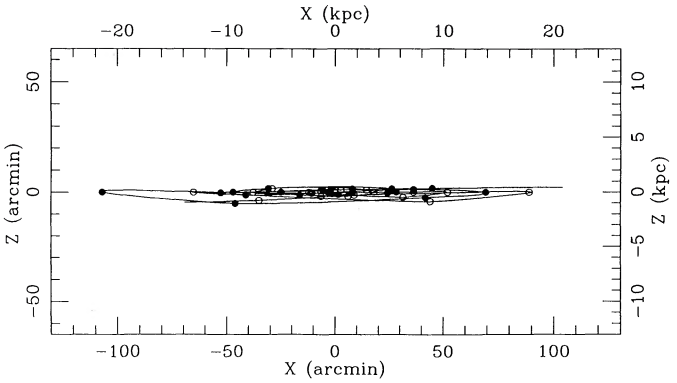

FIG. 10*a*

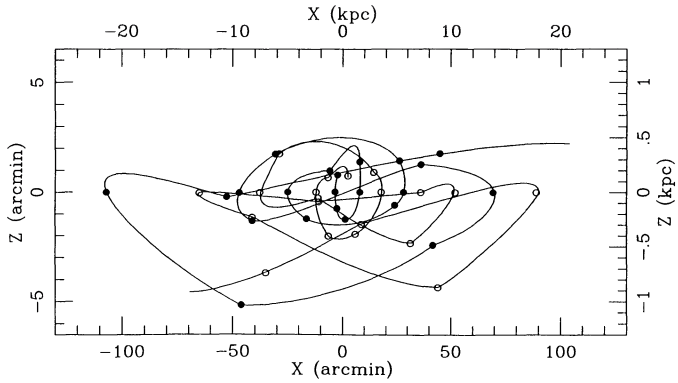

FIG. 10*b*

FIG. 10.—Projected distribution of the midplane with respect to a nominal disk inclination of 78°. The measurement points of Table 3 are indicated with closed and open symbols for arms a–o and A–N, respectively. The solid lines are interpolated values as described in § 3.1. (*a*) Distribution as seen with identical scales in both dimensions. (*b*) Distribution as seen with a 10 times more sensitive scale for out-of-plane departures.

contends, M32 has recently passed through the disk of M31 at a comparable radius.

5.3. *The Distribution of Gas Scale Height*

Since the type of perturbation experienced by M31 is likely to be a common occurrence in other galaxies, substantial care should be taken in the interpretation of gas scale heights and implied "flaring" of gas at large radii observed in apparently edge-on systems. The distribution of disk thickness with radius which we derive in § 2.3 is shown in Figure 11*a*. Since the disk thickness, h is here defined to be the full width to a given column density (2.5 K in 8.2 km s^{-1} giving 3.7 × 10^{19} cm^{-2} for optically thin H I), the corresponding scale height can be derived from a knowledge of the peak column density and an assumed functional dependence. Two different functional forms have commonly been employed to describe the out-of-plane dependence of gas (column) density. A Gaussian form,

$$N_{\rm H}(z) = N_{\rm H}(0)\ \exp\ (-z^2/2s_G^2)\ , \qquad (10)$$

is often used (e.g., Baker & Burton 1975) to describe a cool, dense layer closely confined to the galactic disk, while an exponential form,

$$N_{\rm H}(z) = N_{\rm H}(0)\ \exp\ (-|\,z\,|/s_E)\ , \qquad (11)$$

is more often used (e.g., Lockman, Hobbs, & Shull 1986) to describe a warmer, more extended gas layer. Given the relatively coarse resolution and low column densities we are considering, it seems more appropriate to derive the exponential scale height, s_E, implied by these data. (With more extensive modeling it may be possible to extract the functional form directly from the data.) The scale height implied by the disk thickness h and peak brightnesses T_P assuming low average optical depths is given by

$$s_E = \frac{h}{2}\ln\left(\frac{2.5}{T_P}\right)^{-1}\ . \qquad (12)$$

The well-defined values (where peak brightnesses were more than about 10 K) are plotted in Figure 11*b* against radius. (Gaussian scale heights derived in a similar fashion were comparable, but typically 10% smaller.) There is a roughly linear dependence of scale height on radius with considerable intrinsic scatter. The linear regression solution,

$$s_E = 182(\pm 37) + 16(\pm 3)R_{\rm kpc}\ {\rm pc}\ , \qquad (13)$$

is also plotted in the figure as a dotted line. There are, thus, indications for a modest flaring of the gas layer from a scale height of about 200 pc at 5 kpc to about 600 pc at 25 kpc. As noted above, the midplane offset over this range of radii is comparable, so that failure to account for it would have had a very significant effect on the derived distribution of scale height.

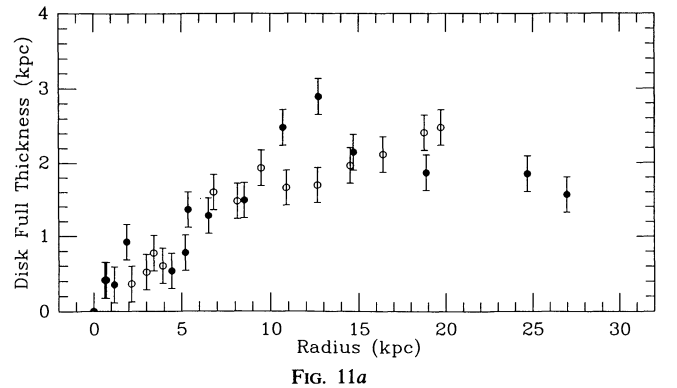

FIG. 11*a*

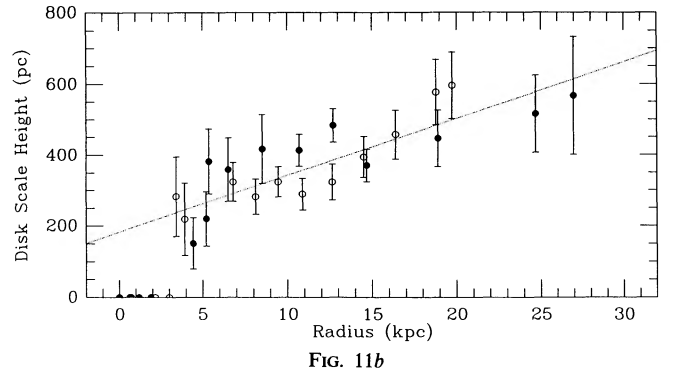

FIG. 11*b*

FIG. 11.—Radial dependence of disk thickness. Values derived from the measurement points of Table 3 are indicated with closed and open symbols for arms a–o and A–N, respectively. (*a*) Full thickness of the gaseous disk at a column density of about 3.7 × 10^{19} cm^{-2} as derived in § 2.3. (*b*) Exponential scale height of the disk as derived in § 5.3. The dotted line is the linear regression fit to the data.

5.4. "*Warps*" *and Massive Dark Halos*

The term "warp" has been used extensively to describe departures from a planar distribution of gas and stars in galactic disks. The term has often been taken to imply a bisymmetric departure of the disk midplane along a fixed line of nodes in both theoretical (e.g., Toomre 1983; Sparke & Casertano 1988) and applied (e.g., Rogstad, Lockhart, & Wright 1974; Brinks & Burton 1984) papers. Midplane departures of M31's disk do not appear to be strictly organized in a bisymmetrical structure. While some degree of bisymmetry is present, the superposed departures over 60°–90° of azimuth have a comparable amplitude, as can be seen in Figures 3, 4, and 10. A similar effect was noted by Kulkarni, Blitz, & Heiles (1982) for the Galaxy, where the "scalloping" (with an azimuthal wavenumber of about 10) has as large an amplitude as the "warp." Sancisi (1983) points out that large asymmetries in midplane departures are in fact the rule rather than the exception for nearby galaxies. In view of the current analysis, it seems questionable whether the concept of a warp offers a useful characterization of the nonplanar gaseous disk of M31.

What becomes very clear from the current study is that spiral arms at a number of distinct radii are heavily overlapped in projection. The most remarkable alignments occur near $(X, Y) = (+30', +10')$ and $(+10', -10')$ in, e.g., Figure 4*b*. In particular, the region at $(+30', +10')$ with gas-rich arms at both 10 and 13 kpc radius has been the subject of some comment (Ryden & Stark 1986; Casoli & Combes 1988), since CO is detected at the velocities of both spiral arms. The previous lack of a good model for the distribution of gas in M31 has led both these authors astray in their interpretation. Ryden & Stark (1986) suggested that the double-peaked CO profiles might be the result of rapid acceleration of the gas in cloud-cloud collisions within a single spiral arm. Casoli & Combes (1988), on the other hand, interpret the more distant spiral arm as lying at a radius of 16–20 kpc on the basis of the warp model of Brinks & Burton (1984). The conclusions concerning the existence of molecular gas in M31 at large radii are rather different with the 13 kpc radius found here.

Another topic worth considering is the question of massive dark halos. As already noted in § 4.2, the rotation curve derived in this study and shown in Figure 8*b* is well fitted by a mass distribution proportional to the blue-light distributions of the stellar bulge and disk with a mass-to-light ratio of 6.5 $M_\odot/L_\odot$. This mass-to-light ratio is easily compatible with a wide range of possible star formation histories in a 10–15 Gyr old system (e.g., Guiderdoni & Rocca-Volmerange 1987) if a "standard" initial mass function (IMF) is adopted and a 50% yield of nonluminous objects (Bahcall, Hut, & Tremaine 1985). There appears to be no indication for the existence of a massive dark halo in M31 out to a radius of at least 28 kpc. This result is in contrast to that found in less rigorous analyses of M31, where proper account of the changing orientation was not taken. It is interesting to speculate on how robust the published rotation curves of nearby galaxies with apparently constant or rising velocities at large radii will be on more careful scrutiny. At the very least, the need to invoke additional dark mass with a more uniform mass distribution than that of the stellar disk is apparently not universal.

6. SUMMARY

Recognition of the kinematic signature of individual spiral arm segments (in § 2) has made possible a very compact, yet quite complete, parameterization of the global neutral hydrogen content of M31, via equation (1) and Table 3. Two continuous, trailing spiral arms (illustrated in Figs. 4 and 5) can be traced from about 0.5 to 27 kpc from the nucleus, which accurately account for the kinematic and spatial distribution of gas. The three-dimensional geometry of the gas distribution has been derived with only limited assumptions concerning axisymmetry of the velocity field: i.e., local axisymmetry (within intervals of about 90° of local azimuth) and inner bisymmetry (within 4 kpc of the nucleus). Significant variations in inclination as a function of azimuth (i.e., local line of nodes) and radius are found, leading to departures of the local midplane from a few hundred parsecs in a tilted disk in the inner galaxy to in excess of a kiloparsec in the "warp" of the outer galaxy (see Figs. 3 and 10). The lack of overwhelming bisymmetry in midplane departures makes the use of the term "warp" somewhat questionable in this context. The distribution of exponential scale height of the gas with radius was found to vary between 200 and 600 pc as illustrated in Figure 11. The spiral pattern in the inner galaxy has an elliptical distortion seen in Figures 6 and 7 which leads to significant corrections to the axisymmetric rotation velocity and implied mass distribution. The consequences of assuming circular and elliptical gas orbits in the inner galaxy are contrasted in Figures 8*a* and 8*b*.

Three regimes of radius emerge from the analysis with distinctive morphological and kinematic properties, as seen in Figures 6 and 7 and Table 2, suggesting that the inner Lindblad resonance occurs near 5.4 kpc, and corotation of the spiral pattern and gaseous disk near 16.3 kpc. Together with the corrected rotation curve of Figure 8*b*, these positions allow derivation of the pattern frequency, $\Omega_p = 15 \pm 2$ km s^{-1} kpc^{-1}, and the likely position of the outer Lindblad resonance.

The rotation curve of M31 is well fitted by a mass distribution which follows the stellar light distribution with a fixed $M/L = 6.5\ M_\odot/L_\odot$. There are no indications for a massive dark halo out to a radius of at least 28 kpc.

It is a pleasure to acknowledge illuminating and enjoyable discussion in the course of this work with Tjeerd van Albada, Thijs van der Hulst, and Bob Sanders. Thanks are due to Kor Begeman for his modification of the rotation-curve–fitting software and to Rene Walterbos for useful suggestions for modifications to the text.

REFERENCES

Arp, H. 1964, ApJ, 139, 1045
Baade, W. 1963, in Evolution of Stars and Galaxies, ed. C. Payne-Gaposchkin (Cambridge: Harvard Univ. Press), 56
Baade, W., & Swope, H. H. 1963, AJ, 68, 435
Bahcall, J. N., Hut, P., & Tremaine, S. 1985, ApJ, 290, 15
Baker, P. L., & Burton, W. B. 1975, ApJ, 198, 281
Begeman, K. 1987, Ph.D. thesis, Univ. of Groningen
Braun, R. 1990, ApJS, 72, 755
Brinks, E. 1984, Ph.D. thesis, Univ. of Leiden
Brinks, E., & Burton, W. B. 1984, A&A, 141, 195
Brinks, E., & Shane, W. W. 1984, A&AS, 55, 1979 (BS84)
Byrd, G. G. 1976, ApJ, 208, 688
———. 1978, ApJ, 226, 70
Casoli, F., & Combes, F. 1988, A&A, 198, 43
Ciardullo, R., Rubin, V. C., Jacoby, G. H., Ford, H. C., & Ford, W. K. 1988, AJ, 95, 438
Cram, T. R., Roberts, M. S., & Whitehurst, R. N. 1980, A&AS, 40, 215
Dressler, A., & Richstone, D. O. 1988, ApJ, 324, 701
Emerson, D. T. 1974, MNRAS, 169, 607 (E74)
Guiderdoni, B., & Rocca-Volmerange, B. 1987, A&A, 186, 1

Henderson, A. P. 1979, A&A, 75, 311
Hodge, P. W. 1979, AJ, 84, 744
Hodge, P. W., & Kennicutt, R. C. 1982, AJ, 87, 264
Kent, S. M. 1987, AJ, 93, 816
Kormendy, J. 1988, ApJ, 325, 128
Kormendy, J., & Norman, C. A. 1979, ApJ, 233, 539
Kulkarni, S. R., Blitz, L., & Heiles, C. 1982, ApJ, 259, L63
Light, E. S., Danielson, R. E., & Schwarzschild, M. 1974, ApJ, 194, 257
Lin, C. C., Yuan, C., & Shu, F. H. 1969, ApJ, 155, 721
Lockman, F. J., Hobbs, L. M., & Shull, J. M. 1986, ApJ, 301, 380
Mihalas, D., & Routly, P. M. 1968, in Galactic Astronomy, ed. G. Burbidge & M. Burbidge (San Francisco: Freeman), 216
Mulder, W. A. 1986, A&A, 156, 354
Pallet, A., Astier, N., Viale, A., Courtes, G., Maucherat, A., Monnet, G., & Simien, F. 1978, A&AS, 31, 439
Roberts, M. S. 1966, ApJ, 144, 639
Rogstad, D. H., Lockhart, I. A., & Wright, M. C. H. 1974, ApJ, 193, 309
Rubin, V. C., & Ford, W. K. 1970, ApJ, 159, 379 (RF70)
Ryden, B. S., & Stark, A. A. 1986, ApJ, 305, 823
Sancisi, R. 1983, in Internal Kinematics and Dynamics of Galaxies, ed. E. Athanassoula (Dordrecht: Reidel), 55
Sanders, R. H., & Huntley, J. M. 1976, ApJ, 209, 53
Sawa, T., & Sofue, Y. 1981, PASJ, 33, 665
Shu, F. H., Milone, V., & Roberts, W. W. 1973, ApJ, 183, 819
Simien, F., Athanassoula, E., Pellet, A., Monnet, G., Maucherat, A., & Courtes, G. 1978, A&A, 67, 73
Sofue, Y., & Kato, T. 1981, PASJ, 33, 449
Sparke, L. S., & Casertano, S. 1988, MNRAS, 234, 873
Stark, A. A. 1977, ApJ, 213, 368
Toomre, A. 1977, ARA&A, 15, 437
———. 1983, in Internal Kinematics and Dynamics of Galaxies, ed. E. Athanassoula (Dordrecht: Reidel), 177
Unwin, S. C. 1980, MNRAS, 192, 259
Visser, H. C. D. 1980, A&A, 88, 149
Walterbos, R. A. M., & Kennicutt, R. C. 1988, A&A, 198, 61